Internal Dynamics Interact with Proprioceptive Feedback During Movement Execution in an RNN Model of Motor Cortex

Hongru Jiang[a,1], Xiangdong Bu[a,1], Zhiyan Zheng[a], Xiaochuan Pan[b] and Yao Chen[a,*]

[a] School of Biomedical Engineering, Shanghai Jiao Tong University, Shanghai, 200240, China
[b] School of Mathematics, East China University of Science and Technology, Shanghai, 200237, China

ARTICLE INFO

Keywords:
Motor cortex
Proprioceptive feedback
Inhibitory stabilized network
Neural population dynamics
Movement Execution

ABSTRACT

The motor cortex initiates movement by sending temporal patterns to down-stream neural circuitry. The patterns during movement execution are thought to arise from the internal dynamics within motor cortical network. However, external inputs such as proprioception also shape motor cortical dynamics. To investigate the contribution of internal dynamics and proprioceptive feedback to voluntary movement execution, we constructed several motor cortex models receiving different combinations of proprioceptive feedback from a virtual arm to perform a delayed reach task. Considering the delay, noise and source of sensory feedback, we construct a sensory estimation network. We found that the inhibitory stabilized network receives hand kinematics and muscle force generated patterns most similar to those observed in motor cortex neuronal data. Furthermore, we used a disruption strategy to dissect the contribution of internal dynamics and proprioceptive feedback, and found that internal dynamics dominate, while proprioceptive feedback fine-tunes motor command. Analysis of the ablation experiment reveals that proprioceptive feedback improves the robustness against noisy initial conditions. Our results highlights that both intrinsic architecture and external input are critical to produce brain-like neural activity.

1. Introduction

Voluntary movement, such as reaching, grasping, and speaking, is central to our interaction with the world. The motor cortex (MC), which orchestrates intricate neural pathways to generate motor command, is critical for planning and executing movement. Electrophysiological recordings in non-human primates have revealed that neuronal activity in the MC represents movement kinematics, including direction (Georgopoulos et al., 1982), velocity (Inoue et al., 2018) and isometric force (Sergio et al., 2005). However, this perspective only partially explains complex single-neuron multiphasic firing rate (Kalaska, 2019).

With advances in recording technologies and computational methods, the focus on MC has shifted from the representation of output to how motor command is created (Figure 1A). Firing rates of all neurons (neural population responses) in MC coordinate patterns for a particular movement. Recent studies have emphasized that MC is a dynamical system where future state depends on its current state and dynamical rule that dictates evolution (Churchland et al., 2012, 2010; Shenoy et al., 2013; Vyas et al., 2020). The dynamics result from the internal dynamics within MC (neuronal connectivity) and external inputs from other areas. Under the dynamical systems view, Churchland et al. (2012) projected population responses into low-dimensional space by their own dimensionality reduction method named jPCA and found rotational dynamics of the MC when monkeys perform reach task. Neural population responses in the state space from different starting point, follow rotational paths in the same direction for all movements. These rotational patterns revealed the simple nature of complex individual neural responses (Churchland et al., 2012). Furthermore, the dynamical system perspective has paved the way for interpreting motor cortical activity via recurrent neural networks (RNNs) — abstract neural computational of interconnected neurons. In one class of models, the MC is approximated as an autonomous dynamical system during movement execution, with negligible external input (Figure 1B) (Churchland et al., 2012; Hennequin et al., 2014; Sussillo et al., 2015; Zimnik and Churchland, 2021; Michaels et al., 2016). Neural population responses evolve from a specific initial condition, defined as the firing rates at movement onset (Afshar et al., 2011; Churchland et al., 2010), under the control of strong internal dynamics within MC. These models not only generate neural responses similar to real data at single-cell level, but also display rotational dynamics at population level (Churchland et al., 2012).

However, the impact of noise on movement execution in autonomous dynamical systems depends on the subspace in which the perturbations occur. Noise in subspaces orthogonal to the movement execution may not interfere with normal movement and can be readily corrected, while perturbations in the output direction can disrupt the intended movement, making the system sensitive to initial conditions in this subspace. However, the autonomous dynamical system is vulnerable to perturbations in output-relevant dimensions and unable to correct errors from an intended movement. The neural state at movement onset can only vary in a limited subspace, fail tolerate large neural variability.

Alternatively, there is a growing recognition of the role that external inputs play in shaping motor cortical activity (Figure 1C). Situated within a vast and distributed brain network, the MC integrates various external inputs, such as sensory feedback (Sauerbrei et al., 2020; Kalidindi et al.,

**Corresponding author
yao.chen@sjtu.edu.cn (Y. Chen)
ORCID(s):

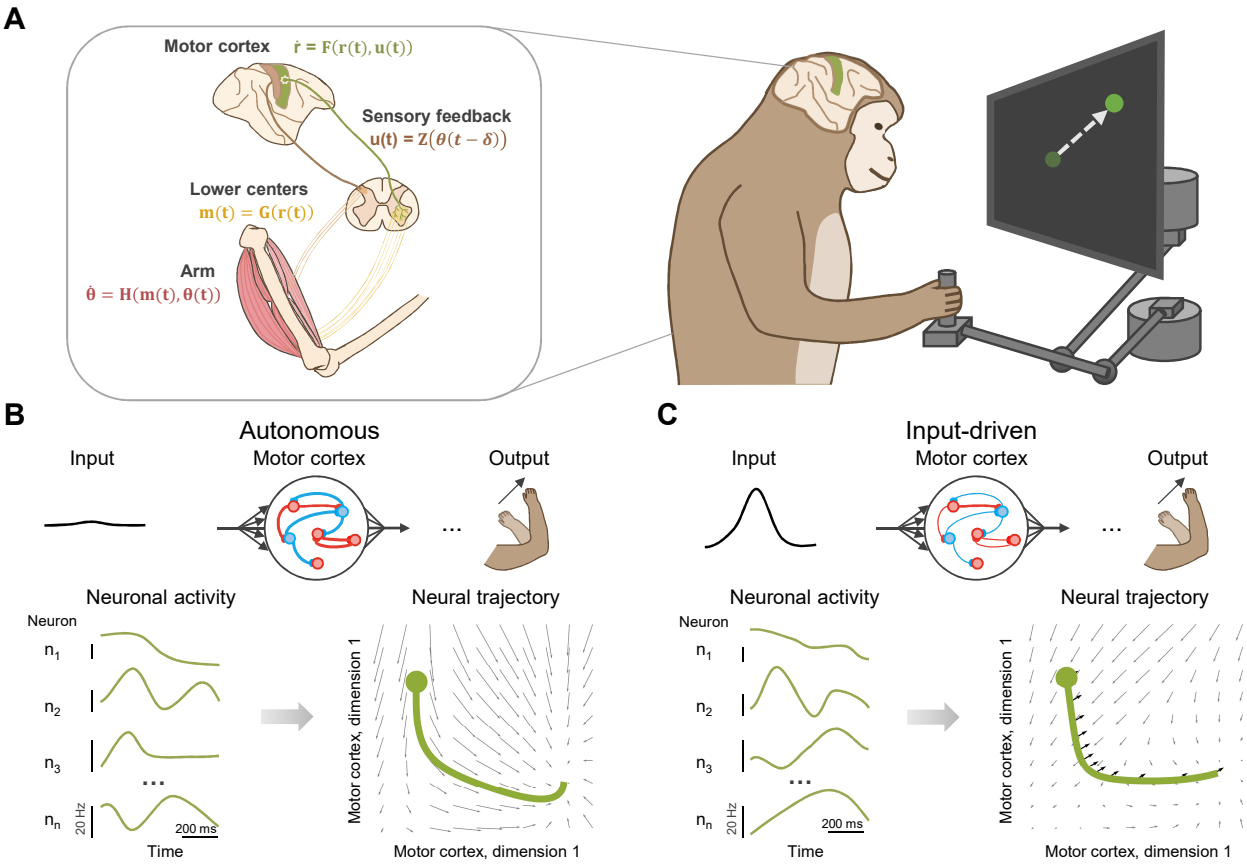

Figure 1: Motor cortex controls reaching under the perspective of dynamical system. (A) Dynamical system perspective on reaching movement. Left: illustration of the delayed reach task. A monkey puts its hand on a planar manipulandum to the center of the workspace to initiate the trial. After a randomized delay, a peripheral target appears, indicating the location the monkey is to reach. Monkey was trained to hold during a variable delay period until a go cue (e.g., auditory signal) prompts the monkey to reach the target. Right: dynamical system model of reaching. Motor cortical firing rates, evolving with a derivative $\dot{r}$, are determined by the internal dynamics in the MC and external input. Firing rates is converted into muscle activity $m(t)$ via a downstream circuit in lower motor centers, thereby updating the joint angles and velocities $\theta(t)$, ultimately reflected in hand movement. Delayed sensory feedback from the arm is sent back to the brain regions outside the MC. (B) MC as an autonomous dynamical system for movement execution. Neuronal population responses is visualized in a low-dimensional state-space, with neural states evolving from specific initial conditions (solid circle) under strong internal dynamics within the MC (grey arrows). The length of arrows illustrates the strength of dynamics. (C) MC as an input-driven dynamical system for movement execution. Neural firing rates starting from the initial condition, are driven by external input (black arrows) and internal dynamics (grey arrows). The internal dynamics are weaker than (C).

2021; Gallego et al., 2020), thalamic (Sauerbrei et al., 2020; Logiaco et al., 2021; Yu et al., 2022) and cerebellar signals (Kumar and Ma, 2023). Sensory feedback is critical in finely controlled movements, as the MC has to integrate multiple sensory information including proprioception, vision and tactile sensation, to generate precise commands. The dynamical system perspective is also reflected in the framework of optimal feedback control (OFC), wherein the MC acts as a feedback controller using the best estimate of sensory feedback to produce motor output (Lillicrap and Scott, 2013; Omrani et al., 2017; Todorov and Jordan, 2002). OFC, which has successfully explained experimental behavior (Scott, 2004; Todorov and Jordan, 2002), is also expected to shape motor cortical dynamics during movement execution (Herter et al., 2009; Perich et al., 2020). A recent study found that sensory feedback also exhibits rotational dynamics, suggesting that sensory feedback may be determinant in cortical pattern generation (Kalidindi et al., 2021). Yet for the complete movement process, this model simplifies the external input as merely sensory information during preparatory period, potentially overstating the contribution of sensory feedback during movement execution.

Our study focuses on proprioceptive feedback, a critical component in motor control. The absence of proprioception leads to significant motor deficits, even when visual feedback is available (Sainburg et al., 1995). Healthy individuals estimate hand motion rely almost on proprioceptive feedback compared to visual feedback (Crevecoeur et al., 2016). In this work, we investigate the interaction between proprioceptive feedback and internal dynamics in the MC during

movement execution base on delayed-reach task. Utilizing the inhibitory stabilized network (ISN) (Hennequin et al., 2014; Kao and Hennequin, 2019), we first built a baseline model that receives the feedback of hand kinematics and muscle force in a noise-free environment. Considering the MC generates motor command in the face of delayed and noisy feedback and receptors in the arm do not encode hand kinematics directly, we then built a sensory estimation network to estimate the proprioception. We incorporate the baseline and sensory estimation into a complete model, which generates firing rates that resembled real data at both single-cell and population levels, both qualitatively and quantitatively. We found the elaborate recurrent structure and proprioceptive feedback are important in motor cortical dynamics. Furthermore, we dissected their contribution by disrupting them at graded percentage of timecourse and found the absence of internal dynamics makes the network 'explode', whereas the absence of proprioceptive feedback led to ceaseless movement. These results suggest internal dynamics are dominant in cortical pattern generation, while proprioceptive feedback is essential for speed control. Additionally, proprioceptive feedback tames sensitivity to initial conditions thus improves robustness of the network.

In summary, our research offers new insights into the intricate interaction between the internal dynamics within MC and proprioceptive feedback during movement execution, potentially reshaping our understanding of motor control.

2. Method

2.1. A model for movement generation

2.1.1. Musculoskeletal Arm model

We constructed a two-link musculoskeletal arm model in the horizontal two-dimensional plane, driven by six lumped muscles (mono-articular shoulder flexors, mono-articular shoulder extensors, mono articular elbow flexors, mono-articular elbow extensors, biarticular flexors and biarticular extensors) (Lillicrap and Scott, 2013). First, muscle activity $\boldsymbol{m}(t)$ was transformed into muscle force $\boldsymbol{f}(t)$ via the force-length-velocity function:

$$\boldsymbol{f}(t) = F_{lv}\boldsymbol{m}(t) \tag{1}$$

where $F_{lv} = F_l(\boldsymbol{l}) \cdot F_v(\boldsymbol{l}, \dot{\boldsymbol{l}})$ is the force-length-velocity function:

$$F_l(\boldsymbol{l}) = \exp\left(-\text{abs}\left(\frac{\boldsymbol{l}^{\beta} - 1}{\omega}\right)^{\rho}\right) \tag{2}$$

$$\mathrm{F}_v(\boldsymbol{l}, \dot{\boldsymbol{l}}) = \begin{cases} \frac{V_{\max} - \dot{l}}{V_{\max} + (c_{V0} + c_{V1})\dot{l}} & \dot{\boldsymbol{l}} \leq 0 \\ \frac{b_V - \left(a_{V0} + a_{V1}l + a_{V2}l^2\right)\dot{l}}{b_V + \dot{l}} & \dot{\boldsymbol{l}} \leq> 0 \end{cases} \tag{3}$$

where $\beta = 1.55$, $\omega = 0.81$, $\rho = 2.12$, $V_{\max} = -7.39$, $c_{V0} = -3.21$, $c_{V1} = 4.17$, $b_V = 0.62$, $a_{V0} = -3.12$, $a_{V1} = 4.21$, $a_{V2} = -2.67$. $\boldsymbol{l} = (l_1, l_2, \ldots, l_6)$ and $\dot{\boldsymbol{l}} = (\dot{l}_1, \dot{l}_2, \ldots, \dot{l}_6)$ are the length and velocity of each muscle, defined as:

$$l_i = 1 + \frac{A_{1i}\left(\theta_{1i}^0 - \theta_1\right)}{L_i^0} + \frac{A_{2i}\left(\theta_{2i}^0 - \theta_2\right)}{L_i^0} \tag{4}$$

$$\dot{l}_i = -\frac{A_{1i}\dot{\theta}_1}{L_i^0} - \frac{A_{2i}\dot{\theta}_2}{L_i^0} \tag{5}$$

where $(\boldsymbol{\theta}, \dot{\boldsymbol{\theta}}) = ((\theta_1, \theta_2)^T, (\dot{\theta}_1, \dot{\theta}_2)^T)$ includes the angles and velocities of the elbow and shoulder joints, which are initialized with the parameters in Table 1 at the trial beginning. $\boldsymbol{A}$ is the moment arm matrix, $\boldsymbol{L^0}$ is the optimal length matrix and $\boldsymbol{\theta^0}$ are the and joint angle, defined as:

$$\boldsymbol{\theta^0} = \frac{\pi}{180}\begin{pmatrix} 15 & 4.88 & 0 & 0 & 4.5 & 2.12 \\ 0 & 0 & 80.86 & 109.32 & 92.96 & 91.52 \end{pmatrix} \tag{6}$$

$$\boldsymbol{L^0} = \begin{pmatrix} 7.32 & 3.26 & 6.4 & 4.26 & 5.95 & 4.04 \end{pmatrix} \tag{7}$$

$$\boldsymbol{A} = \begin{pmatrix} 2 & -2 & 0 & 0 & 1.5 & -2 \\ 0 & 0 & 2 & -2 & 2 & -1.5 \end{pmatrix} \tag{8}$$

The muscle force was subsequently mapped into joint torques $\boldsymbol{j}(t) = \boldsymbol{A}\boldsymbol{f}(t)$. The arm state evolved dynamically according to:

$$\ddot{\boldsymbol{\theta}} = \mathcal{M}(\boldsymbol{\theta})^{-1}\left(\boldsymbol{j}(t) - \mathcal{X}\left(\boldsymbol{\theta}, \dot{\boldsymbol{\theta}}\right) - \mathcal{B}\dot{\boldsymbol{\theta}}\right) \tag{9}$$

where $\mathcal{M}$ is the inertia matrix, $\mathcal{X}$ is the centripetal and Coriolis forces, and $\mathcal{B}$ is the damping matrix representing joint friction. The above parameters are given by

$$\mathcal{M}(\boldsymbol{\theta}) = \begin{pmatrix} a_1 + 2a_2 cos\theta_2 & a_3 + a_2 cos\theta_2 \\ a_3 + a_2 cos\theta_2 & a_3 \end{pmatrix} \tag{10}$$

$$\mathcal{X}\left(\boldsymbol{\theta}, \dot{\boldsymbol{\theta}}\right) = a_2 sin\theta_2 \begin{pmatrix} -\dot{\theta}_2\left(2\dot{\theta}_1 + \dot{\theta}_2\right) \\ \dot{\theta}_1^2 \end{pmatrix} \tag{11}$$

$$\mathcal{B} = \begin{pmatrix} 0.05 & 0.025 \\ 0.025 & 0.05 \end{pmatrix} \tag{12}$$

where $a_1 = I_1 + I_2 + M_2 L_1^2$, $a_2 = M_2 L_1 D_2$, and $a_3 = I_2$. These parameters are given in the Table 1. The hand position, $\boldsymbol{p}$ and velocity, $\dot{\boldsymbol{p}}$ are given by:

$$\begin{pmatrix} p_x \\ p_y \\ \dot{p}_x \\ \dot{p}_y \end{pmatrix} = \begin{pmatrix} \mathrm{L}_1 \cos\theta_1 + \mathrm{L}_2 \cos\theta_a \\ \mathrm{L}_2 \sin\theta_1 + \mathrm{L}_2 \sin\theta_a \\ -\dot{\theta}_1\,\mathrm{L}_1 \sin\theta_1 - \dot{\theta}_a\,\mathrm{L}_2 \sin\theta_a \\ \dot{\theta}_1\,\mathrm{L}_1 \cos\theta_1 + \dot{\theta}_a\,\mathrm{L}_2 \cos\theta_a \end{pmatrix} \tag{13}$$

where $\boldsymbol{p} = (p_x, p_y)^T$, $\dot{\boldsymbol{p}} = (\dot{p}_x, \dot{p}_y)^T$, and $\theta_a = \theta_1 + \theta_2$.

2.1.2. Inhibition-stabilized network

We modeled the MC as an biologically plausible network, inhibition-stabilized network (ISN), satisfying Dale's law (neurons are either excitatory or inhibitory) (Hennequin et al., 2014; Eskikand et al., 2023). ISN can produce rich and naturalistic neural responses, similar to real neural firing rates. Our network comprised 150 excitatory and 50 inhibitory neurons (N=200 neurons) with a similar neuron proportion to that in the MC of non-human primates (Bakken et al., 2021; Chen et al., 2023).

Initially, we constructed a random connectivity matrix of size $N \times N$ with a connectivity density $p = 0.1$. The non-zero excitatory weights were drawn from a lognormal distribution with mean $log(w_0)$ and variance 1, where $w_0^2 = r^2/(p(1-p))$ and r represents the initial spectral abscissa. For inhibitory weights, we employed a uniform distribution between -1 and 0. r is set to 1.2 for the (closed-loop) network receiving proprioceptive feedback.

The random excitatory weights are stabilized by fine-tuned inhibitory architecture (Hennequin et al., 2014). We optimized the inhibitory synapses to minimize the "smoothed spectral abscissa" α_ϵ, the greatest real part of $\boldsymbol{W}$'s eigenspectrum, to below 0.9. The gradient of smoothed spectral abscissa with respect to the connectivity matrix W is expressed as

$$\frac{d\alpha_\epsilon(\boldsymbol{W})}{d\boldsymbol{W}} = \frac{\boldsymbol{OP}}{tr(\boldsymbol{OP})} \tag{14}$$

where $\boldsymbol{O}$ and $\boldsymbol{P}$ are respectively the observability and controllability Gramians of the system, defined as:

$$\begin{aligned} \boldsymbol{O} &= \frac{2}{\tau}\int_0^\infty e^{(\boldsymbol{W}^T-\boldsymbol{I})t/\tau} e^{(\boldsymbol{W}-\boldsymbol{I})t/\tau} dt \\ \boldsymbol{P} &= 2\int_0^\infty e^{t(\boldsymbol{W}-\boldsymbol{I})} e^{t(\boldsymbol{W}-\boldsymbol{I})^T} dt \end{aligned} \tag{15}$$

where $\boldsymbol{I}$ is the unit matrix. $\boldsymbol{O}$ and $\boldsymbol{P}$ can be solved from Lyapunov equation.

2.1.3. Initial conditions

Neural firing rates at movement onset significantly determines motor behavior (Pandarinath et al., 2018; Churchland et al., 2010). The movement-specific initial conditions, denoted as $\boldsymbol{x}^* = \left(\boldsymbol{x}_1^*, \boldsymbol{x}_2^*, \ldots, \boldsymbol{x}_8^*\right)$, is defined as:

$$\boldsymbol{x}_k^* = \boldsymbol{x}_{sp} + \sum_{i=1}^{2} \boldsymbol{b}^t{}_i p_{k,i}^* + \sum_{i=1}^{N} Z_{k,i}\boldsymbol{a}_i = \boldsymbol{x}_{sp} + \boldsymbol{\Delta x}^t + \boldsymbol{\Delta x}^* \tag{16}$$

where $\boldsymbol{x}_{sp}$ is the spontaneous activity sampled from Gaussian distribution $\mathcal{N}(20, 9)$ throughout all task phases. $\boldsymbol{p_k}^*$ is the target position with the angle of θ_k^{targ} and the distance of 15 cm from the origin (see in Table 1), $\boldsymbol{b}^t{}_i$ is an N dimensional weight vector sampled from Gaussian distribution $\mathcal{N}(0, 1/I)$. $I = 10$ is the number of the external input. $\boldsymbol{a}$ is the network's orthogonal input directions, and $\boldsymbol{Z}$ is a weight matrix sampled from Gaussian distribution $\mathcal{N}(0, 1.5/N)$. This allows us to detach the input of target position and find diverse range of initial conditions that evoke various transient responses.

The transient responses is quantified by the evoked energy $E(a)$ (Hennequin et al., 2014), defined as:

$$\boldsymbol{E}(\boldsymbol{a}) = \boldsymbol{a}^T\boldsymbol{Oa} \tag{17}$$

The full eigenvectors of $\boldsymbol{O}$, ordered by decreasing eigenvalues, denoted as $\left(\boldsymbol{a_1}, \boldsymbol{a_2}, \ldots, \boldsymbol{a_N}\right)^T$ are the N orthogonal input directions that each maximize the evoked energy. Following Kao et al. (2021), we scale the variance of firing rates after go cue to $\sigma_{reach}^2 = 16$ Hz.

2.1.4. Modeling framework

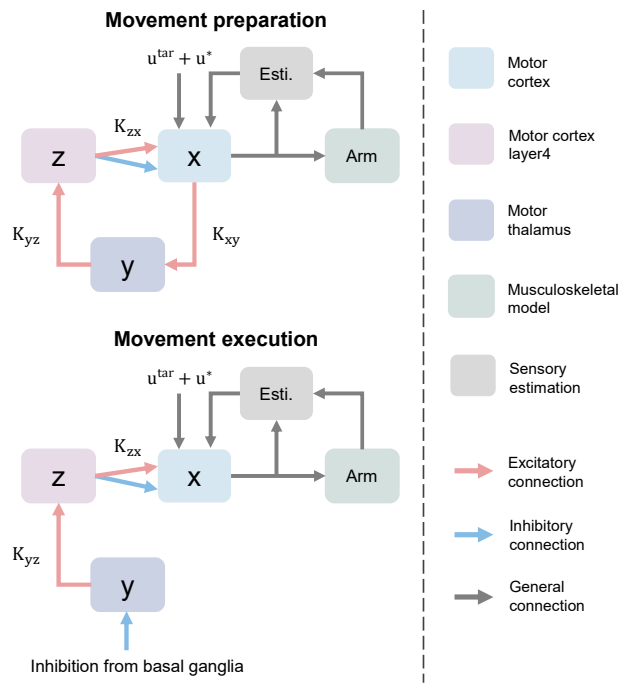

Figure 2: Schematics of thalamocortical circuit model for the delay reach task.

We utilized the gated thalamocortical circuit model, which enables fast preparation and explains the observed orthogonality between preparatory and movement neural activity (Kao et al., 2021) (Figure 2). The simulation was divided into two epochs by the gated action of basal ganglia: the preparation-epoch (before go cue) where basal ganglia disinhibited thalamic neurons, leaving them to interact with cortex (Figure 2A). The execution-epoch (after go cue) where basal ganglia inhibited thalamic neurons and opened the loop (Figure 2B). Furthermore, several constraints were implemented to ensure both biological plausibility and computational feasibility: (1) the MC was divided into the MC and the MC layer 4, and all the connection in the circuit satisfied Dale law. (2) integration dynamics in the thalamus and the MC layer 4 is omitted. (3) muscle activity was artificially set to 0 during movement preparation, bypassing spinal cord modeling for posture control. The corresponding

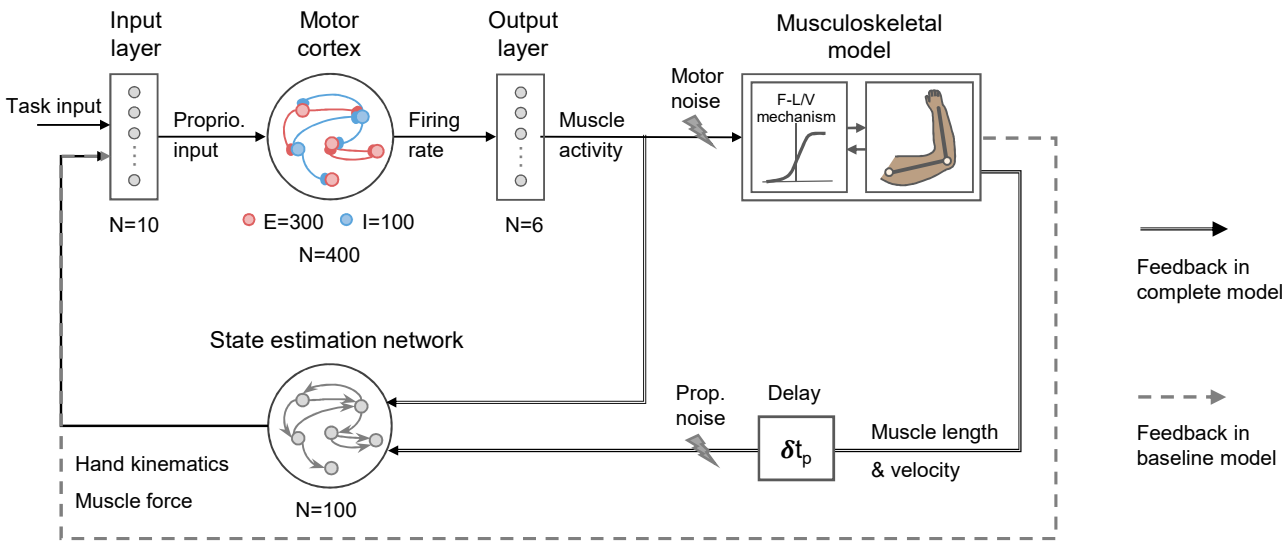

Figure 3: Schematics of the MC network model during movement execution. MC receives task and proprioceptive inputs during movement execution. The firing rates generated by MC network are translated into muscle activity via the output layer. Then, the noisy muscle activity is converted into muscle force through F-L/V mechanism, actuating the motion of the two-link arm model. The baseline model is in an ideal situation where proprioceptive input is from hand kinematics and force directly without any noise and delay. On the other hand, the complete model receives proprioceptive input estimated from delayed and noisy proprioceptive feedback via the sensory estimation network.

dynamics of our circuit model can be described as:

$$\begin{aligned} \tau \frac{d\boldsymbol{x}}{dt} &= -\boldsymbol{x}(t) + \boldsymbol{W}\,[\boldsymbol{x}(t)]^{+} + \boldsymbol{\zeta}(t) + \boldsymbol{u}^{*} + \boldsymbol{u}^{t} + \boldsymbol{K}_{xz}\,[\boldsymbol{z}(t)]^{+} \\ \frac{d\boldsymbol{z}}{dt} &= -\boldsymbol{z} + \boldsymbol{K}_{zy}\,[\boldsymbol{y}(t)]^{+} \\ \frac{d\boldsymbol{y}}{dt} &= -\boldsymbol{y} + \boldsymbol{K}_{yx}\,[\boldsymbol{x}(t)]^{+} \end{aligned} \tag{18}$$

where $\boldsymbol{x}$, $\boldsymbol{y}$, $\boldsymbol{z}$ are the neural activations of MC, MC-layer4 (MC-L4) and thalamus, respectively. $[]^{+}$ is the ReLU Activation Function. $\boldsymbol{K}_{xz}$ is the MC-L4 to MC connectivity matrix, $\boldsymbol{K}_{zy}$ is the thalamus to MC-L4 connectivity matrix, $\boldsymbol{K}_{yx}$ is the MC to thalamus connectivity matrix. Note, $\boldsymbol{K} = \boldsymbol{K}_{xz}\boldsymbol{K}_{zy}\boldsymbol{K}_{yx}$ summarizes these three connectivity matrices around the loop into one feedback gain matrix, which can be calculated from the method described in (Kao et al., 2021).

For the dynamics of MC, $\tau = 200$ is the time constant of MC dynamics. $\boldsymbol{W}$ is the recurrent weight matrix obtained in 2.1.2. $\boldsymbol{\zeta}(t) = \boldsymbol{z}_{sp} + \boldsymbol{z}_{ci} + \boldsymbol{z}_{pp}$ denotes all the inputs. $\boldsymbol{z}_{sp(t)} = \boldsymbol{x}_{sp} - \boldsymbol{W}[\boldsymbol{x}_{sp}]^{+}$ maintains the spontaneous activity of the network. $\boldsymbol{z}_{ci}$ is the condition-independent signal, appears after the go cue and induces a substantial change in dynamics (Kaufman et al., 2016; Kao et al., 2021):

$$\boldsymbol{z}_{ci}(t) = \boldsymbol{a} \times \begin{cases} exp\left(\frac{t_{\text{go}}-t}{600}\right) - exp\left(\frac{t_{\text{go}}-t}{60}\right) & t > t_{\text{go}} \\ 0 & t \leq t_{\text{go}} \end{cases} \tag{19}$$

where $\boldsymbol{a} = 7.28 + \boldsymbol{\zeta}$. $\boldsymbol{\zeta}$ is a N dimensional vector sampled from Gaussian distribution $\mathcal{N}(0, 0.2)$. t_{go} is the time when go cue onset. As the $\boldsymbol{x}^{*} > 0$ at go cue, the network could be approximated as a linear dynamical system. Thus, the input $\boldsymbol{u}^{t}$ denoting the target position is defined as:

$$\boldsymbol{u}^{t} = \alpha \times (\boldsymbol{\Delta x}^{t} - \boldsymbol{W}\boldsymbol{\Delta x}^{t}) \tag{20}$$

where $\alpha = 2.7$ is hyper-parameters. The control input defined as:

$$\boldsymbol{u}^{*} = \boldsymbol{x}^{*} - (\boldsymbol{W} + \boldsymbol{K})[\boldsymbol{x}^{*}]^{+} - \boldsymbol{z}_{pp} - \boldsymbol{z}_{sp} - \boldsymbol{u}^{t} \tag{21}$$

was switched off at go cue onset. $\boldsymbol{z}_{pp}$ is the proprioceptive input specified in next subsection.

Finally, MC are readout into muscle activity through a output layer, defined as:

$$\tau_{m}\frac{d\boldsymbol{m}}{dt} = -\boldsymbol{m}(t) + [\boldsymbol{C}\boldsymbol{r}(t)]^{-} \tag{22}$$

where the readout weight matrix $\boldsymbol{C}$ is sampled from Gaussian distribution $\mathcal{N}(0, 0.2^{2}/N)$, and $\tau_{m} = 50$ ms is the time constant. $[]^{-}$ is the LeakyReLU Activation Function with negative slope equal to 0.4. Movement-period neural activity in MC lead the motion of the hand by 150 ms.

2.1.5. *Inputs to the network and sensory estimation*

The MC network received a ten-dimensional estimated proprioceptive input $\boldsymbol{I}_{p}$ including hand position $\boldsymbol{p}_{est}$, and velocity $\dot{\boldsymbol{p}}_{est}$, and muscle force $\boldsymbol{f}_{est}$:

$$\boldsymbol{I}_{p} = (\boldsymbol{p}_{est}{}^{T}, \dot{\boldsymbol{p}}_{est}{}^{T}, \boldsymbol{f}_{est}{}^{T}/\alpha)^{T} \tag{23}$$

Thus, the proprioceptive input is denoted as:

$$\begin{aligned} \boldsymbol{I}_{pp} &= \alpha \times (\boldsymbol{B}\boldsymbol{I}_{p} + \boldsymbol{b}_{b}) \\ \boldsymbol{z}_{pp} &= \boldsymbol{W}\boldsymbol{I}_{pp} - \boldsymbol{I}_{pp} \end{aligned} \tag{24}$$

where $\boldsymbol{B}$ is an $N \times 10$ weight matrix sampled from Gaussian distribution $\mathcal{N}(0, 1/10)$. Note, the first two columns of $\boldsymbol{B}$ are the $\boldsymbol{b^t}_1$ and $\boldsymbol{b^t}_2$ in the 2.1.3. Thus the MC network thus compared the current hand position to the target position (explained in the appendix). $\boldsymbol{b_b}$ is the bias.

In order to estimate the proprioception from the noisy and delayed proprioceptive feedback and the efference copy of the motor command (muscle activity), we constructed a sensory estimation network based on the gated recurrent unit (GRU) with 200 units. GRU is a streamlined version of the LSTM that often achieves comparable performance but faster computation (Chung et al., 2014). The input to GRU is defined as:

$$\begin{aligned} \boldsymbol{p_t} &= ((\boldsymbol{l}_{t-\delta_p} - \boldsymbol{l^0} + \xi_p)^T, (\dot{\boldsymbol{l}}_{t-\delta_p} + \xi_p)^T) \\ \boldsymbol{x_t} &= (\boldsymbol{p}_t^T, \boldsymbol{m}_t^T)^T \end{aligned} \tag{25}$$

where l is the muscle length $\dot{l}$ is muscle velocity, and l^0 is the muscle length at the trial beginning. $\delta_p = 35$ ms, as the proprioceptive feedback takes at least 35 ms to reflect on the motor cortical population activity (Pruszynski et al., 2014). ξ_p is the sensory noise (specified in 3.5).

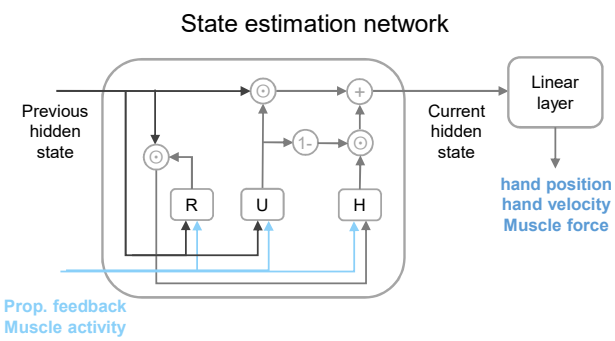

Figure 4: Schematics of sensory estimation network.

The GRU consists of two gates: the reset gate and the update gate (Figure 4). The reset gate controls how much of the previous state to remember, while the update gate determines how much of the new state is a copy of the previous state. For the the hidden state of the previous time step, $\boldsymbol{h_{t-1}}$, the reset gate $\boldsymbol{r_t}$ and update gate $\boldsymbol{u_t}$ are computed as follows:

$$\begin{aligned} \boldsymbol{r_t} &= \sigma(\boldsymbol{W_{rx}x_t} + \boldsymbol{W_{rh}h_{t-1}} + \boldsymbol{b_r}) \\ \boldsymbol{u_t} &= \sigma(\boldsymbol{W_{ux}x_t} + \boldsymbol{W_{uh}h_{t-1}} + \boldsymbol{b_u}) \end{aligned} \tag{26}$$

where $\boldsymbol{W_{rx}}$, $\boldsymbol{W_{ux}}$, $\boldsymbol{W_{rh}}$ and $\boldsymbol{W_{uh}}$ are weight parameters.$\boldsymbol{b_r}$ and $\boldsymbol{b_u}$ are bias. σ is the Sigmoid function.

Then, the candidate hidden state $\tilde{\boldsymbol{h}}_t$ at time t are computed as:

$$\tilde{\boldsymbol{h}}_t = \tanh\left(\boldsymbol{W_{hx}x_t} + \boldsymbol{W_{hh}}\left(\boldsymbol{r_t} \odot \boldsymbol{h}_{t-1}\right) + \boldsymbol{b_h}\right) \tag{27}$$

where $\boldsymbol{W_{hx}}$ and $\boldsymbol{W_{hh}}$ are weight parameters. $\boldsymbol{b_h}$ is bias. $\boldsymbol{h}$ is bias. $\odot$ the Hadamard (elementwise) product operator. The final GRU update equation is defined as:

$$\boldsymbol{h_t} = \boldsymbol{Z_t} \odot \boldsymbol{h}_{t-1} + \left(1 - \boldsymbol{u_t}\right) \odot \tilde{\boldsymbol{h}}_t \tag{28}$$

The hidden state is linear readout into output $\boldsymbol{o_t}$ that are composed of the estimated hand velocity $\boldsymbol{v_{est}}$ and muscle force $\boldsymbol{f_{est}}$:

$$\boldsymbol{o_t} = \begin{pmatrix} \boldsymbol{v_{est}} \\ \boldsymbol{f_{est}} \end{pmatrix} = \boldsymbol{W_{oh}h_t} + \boldsymbol{b_o} \tag{29}$$

where $\boldsymbol{W_{oh}}$ is weight parameters, and $\boldsymbol{b_h}$ is bias. All the parameters in the GRU were sampled from the $\mathcal{N}(0, 0.01)$

2.2. Network optimization

For computational convenience, we first built a baseline MC network which received the proprioception without delay and noise (Figure 3). We starts the simulation from go cue onset (t_{go}) and utilized the Euler integration with time steps of $dt = 10$ ms. The proprioceptive input in thise model is:

$$\boldsymbol{I_p}(t) = (\boldsymbol{p}(t-1)^T, \dot{\boldsymbol{p}}(t-1)^T, \boldsymbol{f}(t-1)^T/\alpha)^T \tag{30}$$

After training the baseline MC network, we set $dt = 1$ ms and obtained the muscle and hand kinematics, which were used for training the sensory estimation network. Finally, we incorporated the baseline MC network and sensory estimation network into a complete MC model, and started the simulation from the beginning of trial (MC at spontaneous activity). The complete model was also simulated by Euler integration with time steps of $dt = 1$ ms.

2.2.1. *Training the baseline motor cortex network*

In the reach task, the network was required to control the arm model to reach the target within 1000 ms after go cue. We first train a baseline motor cortex network considering the absence of the sensory and motor noise using the Adam optimizer with a learning rate of $2\times10^{-}4$ and 1000 iterations. Before optimization, the initial conditions x_k^* and spontaneous activity x_{sp} were restricted in the nullspace of $\boldsymbol{C}$ to prevent movement from occurring at the end of preparation and spontaneously. The loss function are composed of the MSE between the network output and the target at the end of the movement, and a penalization term:

$$\mathrm{L} = \frac{1}{8}\left(\mathrm{L}_0 + \mathrm{L}_1 + \mathrm{L}_2\right) \tag{31}$$

First, the network should hold the arm model for a $\mathrm{T}_0 =$ 300 ms after reaching the target, where hand velocity is nearly zero.

$$\mathrm{L}_0 = \frac{1}{T_0}\sum_{k=1}^{8}\int_{\mathrm{t_{end}}-T_0}^{\mathrm{t_{end}}} \left\|\boldsymbol{p}_k(t) - \boldsymbol{p}_k^*\right\|^2 + \left\|\dot{\boldsymbol{p}}_k(t)\right\|^2 dt \tag{32}$$

where k is the number of movement condition and $\mathrm{t_{end}} =$ 1200 ms. Moreover, we also penalized muscle activity to prevent undue muscle output at the end of the movement:

$$\mathrm{L}_1 = \frac{1}{T_1}\sum_{k=1}^{8}\int_{\mathrm{t_{end}}-T_1}^{\mathrm{t_{end}}} \left\|\boldsymbol{m}_k(t)\right\|^2 dt \tag{33}$$

where $T_1 = 200$ ms.

Second, L_2 regularized the neural dynamics in a low-dimensional space by principal component analysis(PCA), defined as:

$$L_2 = \alpha R_o + \beta R_n \tag{34}$$

where $\alpha = 9 \times 10^{-3}$, $\beta = 10^{-4}$ are the penalization weights.

The first term penalizes oscillation in the first two principle components (PCs), as we observed that the first two PCs of real data are generally α-shaped:

$$R_o = \frac{1}{T_h} \sum_{k=1}^{8} \sum_{i=1}^{2} \int_{t_{go}}^{t_{go}+T_h} \left\| s_{k,i}(t) - s_{k,i}(t_{go} + T_h - t) \right\|^2 dt \tag{35}$$

where $s_i, (i = 1, 2)$ is the first two PCs. $T_h = 420$ ms.

The second term penalizes the temporal distribution of the sixth to the tenth principle components (PCs). If there was no penalization, these PCs would quickly decay to zero. Thus, we required that the value of these PCs at the first half of movement was no stronger than that of the latter half:

$$R_n = \frac{1}{T_h} \max\left(0, \sum_{k=1}^{8} \left(\int_{t_{go}}^{t_{go}+T_h} \left\| s_{k,i=6,\ldots,10}(t) \right\|^2 dt - \int_{t_{go}+T_h}^{t_{go}+2T_h} \left\| s_{k,i=6,\ldots,10}(t) \right\|^2 dt \right)\right) \tag{36}$$

The recurrent architecture of the MC remains fixed after 2.1.2. We optimized movement-specific initial condition $\boldsymbol{x}^*$, input weight matrix $\boldsymbol{B}$ and readout matrix $\boldsymbol{C}$ in the standard MC network.

2.2.2. Training the sensory estimation network

After the optimization of the standard motor cortex network, we trained the sensory estimation network to estimate the current hand kinematics and muslce force from proprioceptive feedback and efference copy of the motor command, using the Adam optimizer with a learning rate of 5×10^-4 and 1000 iterations. There is no sensory noise during training (ξ_p). The loss function was the vector norm between the estimated and the actual proprioception:

$$L = \frac{1}{8T} \sum_{k=1}^{8} \int_{t_{go}}^{t_{end}} \left\| o_k(t) - o_k(t)^* \right\|^2 dt \tag{37}$$

where $\boldsymbol{o_k(t)}^*$ is composed of the actual hand velocities and muscle force. The set of parameters to be optimized is $(\boldsymbol{W_{rx}}, \boldsymbol{W_{ux}}, \boldsymbol{W_{rh}}, \boldsymbol{W_{uh}}, \boldsymbol{W_{hx}}, \boldsymbol{W_{hh}}, \boldsymbol{W_{oh}}, \boldsymbol{b_r}, \boldsymbol{b_u}, \boldsymbol{b_h}, \boldsymbol{b_o})$. Sensory noise was not present during training.

2.2.3. Training the complete motor cortex network

We replace the direct proprioceptive feedback of the baseline model by the sensory estimation network. In the real world, arm operates in a relatively unpredictable environment with sensory and motor noise. Therefore, motor noise was added to the motor commands (muscle activity), while sensory noise was added to the proprioceptive feedback:

$$\begin{aligned} \boldsymbol{m}(t) &= \boldsymbol{m}(t) + \boldsymbol{\xi_m} \boldsymbol{m}(t) \\ \boldsymbol{p}(t) &= \boldsymbol{p}(t)s + \boldsymbol{\xi_p} \end{aligned} \tag{38}$$

where $\boldsymbol{\xi_m}$ and $\boldsymbol{\xi_p}$ were randomly sampled from Gaussian distribution $\mathcal{N}(0, 0.05)$. The loss function is defined as:

$$L = \frac{1}{8T} \sum_{k=1}^{8} \int_{t_{end}-T}^{t_{end}} \left\| \boldsymbol{p}_k(t) - \boldsymbol{p}_k^* \right\|^2 + \|\dot{\boldsymbol{p}}(t)\|^2 \, dt \tag{39}$$

where $T = 1200$ ms and $t_{end} = 300$ ms.

Only the initial conditions $\boldsymbol{x}^*$ was optimized, restricted in the nullspace of the readout matrix $\boldsymbol{C}$ and scaled the variance of firing rates during training. We used the Adam optimizer with a learning rate of 3×10^-3 and 50 iterations.

2.3. Statistical analysis

2.3.1. Preprocessing and Principal component analysis

Neural recording were made from the primary motor cortex (M1) and dorsal premotor cortex (PMd) of Macaque monkey C and M using Utah electrode arrays (Gallego et al., 2020; Safaie et al., 2023; Gallego-Carracedo et al., 2022). Here, We analysed one session of the recordings (268 neurons for monkey C, and 98 neurons for monkey M) and obtained the firing rates following the same procedure described in Safaie et al. (2023). We applied a Gaussian kernel ($\sigma = 50$ ms) to the binned square-root transformed spike counts (bin size 30 ms) of each neuron, and excluded neurons whose mean firing rate less than 1 Hz. Firing rates were computed separately for the movement preparation and execution periods: a 1000 ms window starting 200 ms before target onset, and a 1000 ms window starting 300 ms before movement onset.

The movement onset in our model is defined as time when hand velocity begins to change, however, this subtle change is difficult to detect in the experiment. In the analysis of execution period, We set a 1000 ms window starting 250 ms before movement onset, leaving 50 ms for the detectable changes of hand velocity. We perform such temporal alignment in Figure **??**.

We produced a data matrix $\boldsymbol{X} \in \boldsymbol{R}^{n \times ct}$, where n is the number of neurons, c is the number of reach conditions, and t is the number of time points. Then we 'soft' normalized each neuron's firing rate (fr): $fr = fr/(range(fr)+5)$, and mean-centered fr so that each neuron has a zero mean (Churchland et al., 2012). We used Principal component analysis (PCA) to reduce the dimensionality of data $\boldsymbol{X_{red}} \in \boldsymbol{R}^{n \times ct}$, where k is the number of principal components (PCs).

2.3.2. Demixed principal component analysis

Demixed principal component analysis (dPCA) (Kobak et al., 2016; Brendel et al., 2011) utilizing information discarded by PCA, demixing the components tuning to the task parameters. dPCA seeks to find a transformation matrix $\boldsymbol{W}$, which projects the data matrix $\boldsymbol{R}$, onto a lower-dimensional

space $\boldsymbol{X}$ through the equation that $\boldsymbol{X} = \boldsymbol{R}\boldsymbol{W}$, where each row of $\boldsymbol{R}$ indicates the condition and time points of firing rates, each column of $\boldsymbol{W}$ represents a new dimension, and each column of $\boldsymbol{X}$ represents a component of the population response. Importantly, the key difference between dPCA and PCA is that dPCA seeks a transformation that not only captures variance but also aligns the principal components with the conditions or time indicated by the labels. Therefore, dPCA found some components (columns of $\boldsymbol{X}$) varying over time while being constant across conditions, and others varying across conditions while staying constant over time. We divided these two components into: condition-independent and condition-dependent.

In this paper, we performed dPCA on monkey data in a 1020 ms period starting 300 ms before movement onset and extracted the first fifteen components; we ignored noise covariance within trials.

2.3.3. Canonical-correlation analysis

Canonical-correlation analysis (CCA) was to identify the common patterns in firing rates between model and real data. We focused on a 1020 ms period starting 300 ms before movement onset. We first reduce both the model and monkey data onto ten dimensions by PCA. This ensures that correlations were not driven by low-variance data (Sussillo et al., 2015). Subsequently, we computed canonical variables and their correlations within these dimensionally-reduced datasets.

2.3.4. Procrustes analysis

Procrustes analysis is a statistical method used to compare two sets of shape data by minimizing the sum of squared differences between corresponding points in the two sets. The method involves scaling, rotating, and translating one set of data to optimally superimpose it onto the other set. We used Procrustes analysis to compare the PCs of model and real data described in 2.3.3. To assess the goodness of fit, we calculated the Procrustes statistic, which is the sum of the squares of the point-wise differences between the two datasets. A Procrustes statistic of 0 indicates a perfect fit, while 1 indicates a poorer fit.

2.3.5. Population ratio

As illustrated in Figure 7B, C, the population ratio is defined as:

$$\|x_{dis}(t) - x_{sp}\| / \|x_{ctr}(t) - x_{sp}\| \tag{40}$$

where $x_{dis}(t)$ is the neuronal activity in disruption trial, $x_{ctr}(t)$ is the neuronal activity in control trial. We first removed the spontaneous activity and computed the magnitude of the population activity, which is the vector norm across all neurons. We then compared this magnitude to that in control trial, and averaged the ratio across all conditions. The population ratio quantifies the changes of population activity after different disruptions.

3. Results

3.1. Neural dynamics in the network resembles the real data

Our optimized MC network model completes the delayed reach task, with similar behavioral performance across trials but unique behavioral performance within a single trial (Figure 5A, A1A). The firing rates of individual neurons separated across movement conditions were similar to those observed in monkey the MC data: some neurons display homogeneous, while others display multiphase and heterogeneous firing pattern after movement onset (Figure 5B).

To examined the main characteristics of the population response, we identified condition-independent (identical across conditions) and condition-dependent (condition specific) components of the population response during the transition from preparing to executing a reaching (in a 1s window starting before movement onset) via dPCA (Brendel et al., 2011; Kobak et al., 2016). dPCA explains nearly the same amount of variance as PCA on both monkey and model data (top of Figure 5C, E). Condition-independent components capture 54 % variance of monkey C data, 55 % variance of model data (bottom of Figure 5C, E), indicating that the variance contribution of components from real data and model are highly consistent. These results are comparable to the previous finding that the largest component in motor cortical activity is condition-independent (Kaufman et al., 2016). The two labeled components of model and real data also rank in a similar order. Additionally, the temporal evolution of individual demixed principal components of monkey and model are qualitatively similar (Figure 5D, F). For the condition-independent components, the first component displays rapid rise before movement onset and slow decay after that, while the second exhibits a bump before movement onset and then decay. The third component of monkey and model are almost identical. For the condition-dependent components, the absolute values of the first two components increase after movement onset then decrease, while the sign of the third component inverses during movement execution. Besides, the model's overall trends of components also closely mirror the trends in monkey M data. However, the largest component in monkey M data is condition-dependent (Figure A1B, C), as most of the recorded neurons are heterogeneous.

Moreover, the MC network also display some temporal patterns that are comparable to previous studies in monkeys during reaching. First, we found the a ring-like structure when performing PCA on the firing rate −50 ms before go cue (Figure A1B), as reported by Even-Chen et al. (2019). Second, the MC network displays rotational dynamics (Figure (Churchland et al., 2012)A), similar to those in the real data (Figure A2). However, the fitting quality is low in monkey data (Figure (Churchland et al., 2012)B). This might be attributed to the window for analysis and the identification of the time that movement onset.

In summary, our MC network model has successfully replicated key features of MC activity in reach task, setting

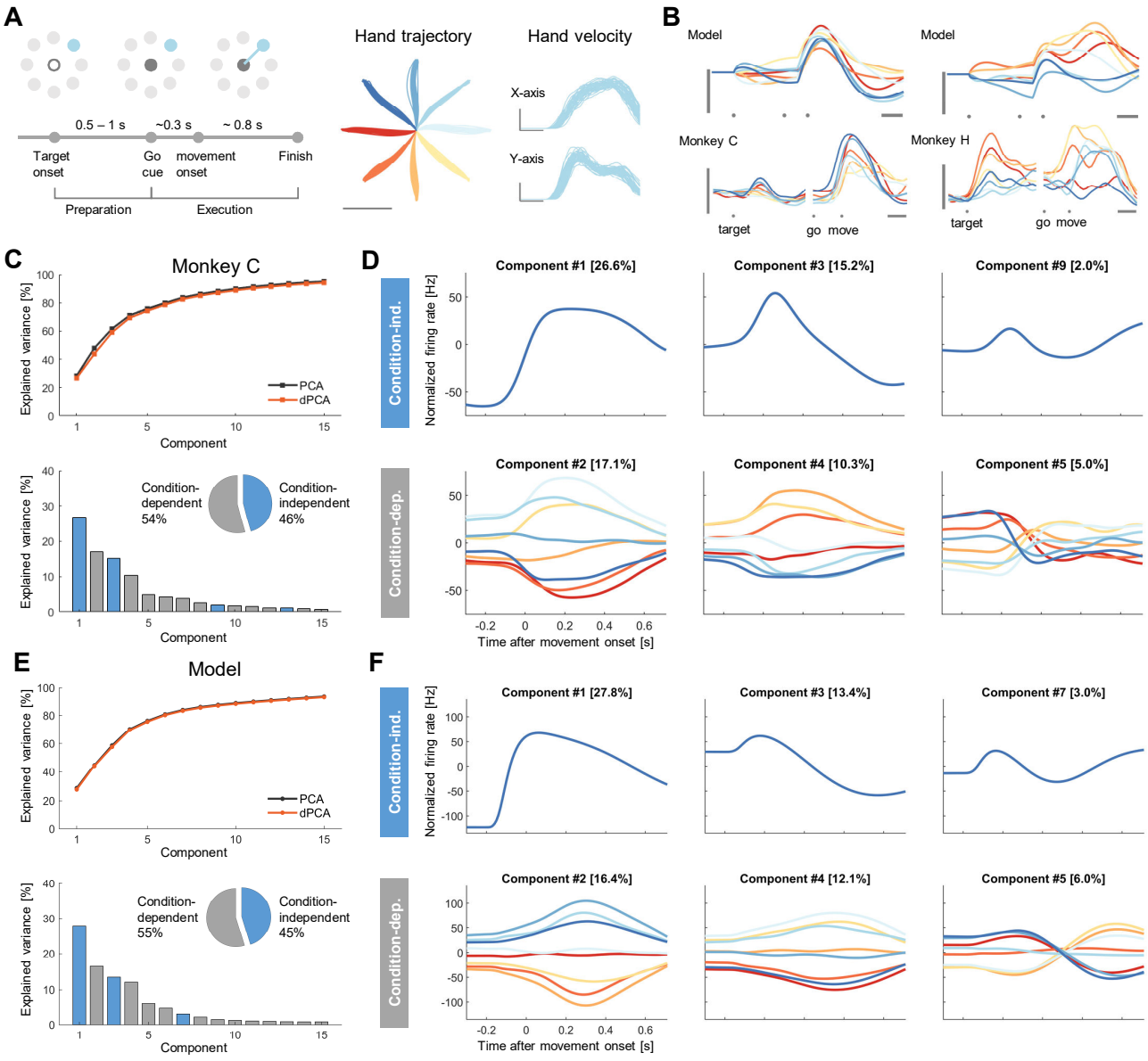

Figure 5: Neural population dynamics of monkey and model during reaching. (A) The simulation of the delayed reach task. Left: the schematic of the task indicating important time point and period for analysis. Middle and right: Behaviour performance of the model. hand trajectories (middle) from 40 trials; horizontal bar: 0.1 m. X and Y hand velocities of the upper-right movement condition after go cue(right); vertical bar: 0.1 m/s, and horizontal bar: 200 ms. (B) Firing rates of representative neurons in the model and monkey. Traces are colored according to the hand trajectories. Vertical bar: 20Hz, and Horizontal bar: 200 ms. (C) Variance captured by dPCA components for monkey C data. Top: cumulative variance explained by dPCA (black) and PCA (orange). Bottom: bars show the variance of the individual demixed principal components. Gray for condition-independent signal, and blue for condition-dependent signal. Pie chart shows the proportions of each signal. (D) Demixed principal components for monkey C data. Top: first three components for condition-independent signal. Bottom: first three components for condition-dependent signal. (E) Same as (C) except for model data. (F) Same as (D) except for model data.

the first stage for further investigations into the cortical pattern generation.

3.2. Further comparison of models and data

So far we have shown the similarity between model and real data at the single-neuron and population level. To directly compare model and real population response and quantify their similarity, we first applied CCA, which finds the common patterns between the two reducted datasets. We found model and monkey C data matched strongly with consistent canonical correlations in the first five PCs (Figure 6B, left); model and monkey M data matched strongly in the first four PCs (Figure 6B, left). Our model explained similar neural variance as monkey data (right of Figure 6B, Figure 6B). The average canonical correlation between monkey C and M is 0.81. The average canonical correlation

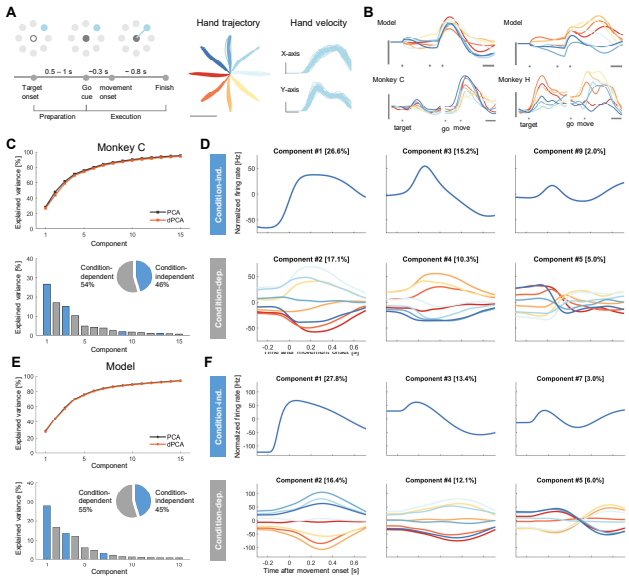

Figure 6: Comparison of the simulated and real population responses. (A) Eigenspectrum of connectivity matrices of ISN (left), autonomous (middle) and random (right) model. The vertical dashed line is the boundary between stability and instability. (B) Left: summary of canonical correlations. ISN, random, autonomous model and monkey M data is compared with the monkey C data separately. Right: cumulative variance explained by PCA for monkey M data and each model. (C) Different combinations of proprioceptive feedback result in three sub-models. (D) Same as (B) except for three sub-models. (E) The similarity between the simulated and real data. Colored filled bars show the average canonical coefficients, and stripes filled bars show the Procrustes statistic. Left for the models in Figure (B), and right for the models in (D).

between model and monkey C (monkey M) is 0.78 (0.73) (Figure 6E, left). Moreover, we also used Procrustes analysis (PA) to compare the similarity between model data and real data, by minimizing Procrustes statistic, which is the sum of squares of the pointwise differences between two datasets. The Procrustes statistic of monkey C and H is 0.24, and the Procrustes statistic of model and monkey C (monkey M) is 0.23 (0.27) (Figure 6E, left). These results demonstrate our model is in good agreement with the MC.

Then we ask is the sophisticated architecture of ISN resembles the dynamics in MC, or proprioceptive feedback is the key factor of motor cortical dynamics? To investigate the contribution of internal dynamics and proprioceptive feedback in the MC model, we built a random network whose recurrent connectivity is sampled from the Gaussian distribution $\mathcal{N}(0, 1/N)$, and an autonomous network which dose not receive proprioceptive feedback (Figure 6A). Theses networks are less similar to the monkey (left of Figure 6B, Figure 6A). The random network explained too much neural variance while the autonomous network explained too little (right of Figure 6B, Figure 6A). The average canonical correlation between random network and monkey C (monkey M) is 0.64 (0.65), and Procrustes statistic for monkey C and H are 0.32. The average canonical correlation between autonomous network and monkey C (monkey M) is 0.66 (0.69), and the Procrustes statistic of model and monkey C (monkey M) is 0.43. We also applied dPCA to the firing rates of random and autonomous network (Figure A4). For the results of random network, the trend of the first condition-independent component was altered, and third condition-independent component disappears; the changes in the first condition-dependent component lag behind that in the real data. For the results of autonomous network, fluctuations in the condition-dependent component are suppressed. Therefore, both the ISN and proprioceptive feedback contribute to motor cortical generation.

Furthermore, we designed an ablation experiment of proprioceptive input by building three sub-models: a model without muscle force (sub-model 1), a model without angular velocity (sub-model 2), a model with only joint angles (sub-model 3) (Figure 6C). The results show that all the sub-models achieved less similarity than the model (Figure 6D, Figure 6B). Specifically, the average canonical correlation between sub-model 1 and monkeys is slightly lower than the model, with 0.74 (monkey C) and 0.7 (monkey M), and Procrustes statistic slightly higher than the model, with 0.26 (monkey C) and 0.28 (monkey M). The neural variance explained by sub-model 1 is also similar to the real data. On the other hand, the canonical correlations and neural variance for sub-model 2 and 3 are comparable: The average canonical correlation between sub-model 2 and monkey C (monkey M) is 0.64 (0.63), and Procrustes statistic is 0.35 (0.37). The average canonical correlation between sub-model 3 and monkey C (monkey M) is 0.62 (0.64), and Procrustes statistic are both 0.37. These two models are less similar to the real data. Additionally, we also applied dPCA to the firing rates of these sub-models (Figure A5). The results of sub-model 1 are comparable to the model, while the neural variance and changes after movement onset of the first condition-dependent component are reduced.

The qualitative resemblances validated our model's capability in capturing the main aspects of neural population dynamics in MC. Lack of fine-tuned recurrent dynamics and proprioceptive feedback would reduce the similarity between model and data. Thus, both the inhibition-stabilized circuit and proprioceptive feedback are essential in cortical pattern generation.

3.3. Internal dynamics dominates in neural population dynamics

The above Motor cortical dynamics are generated by internal dynamics and proprioceptive feedback. What are the relative importance of them during movement execution? Is the movement execution exhibit a bias toward to internal dynamics or proprioceptive feedback? To dissect their contribution, we set internal dynamics (proprioceptive feedback) to zero while keeping proprioceptive feedback (internal dynamics) intact. This disruption strategy occurred 25%, 33%, 50%, 100% timecourse at equal time intervals after go cue onset (Figure 7A). Notably, the motor and sensory noise are set to zero as to prevent other interference

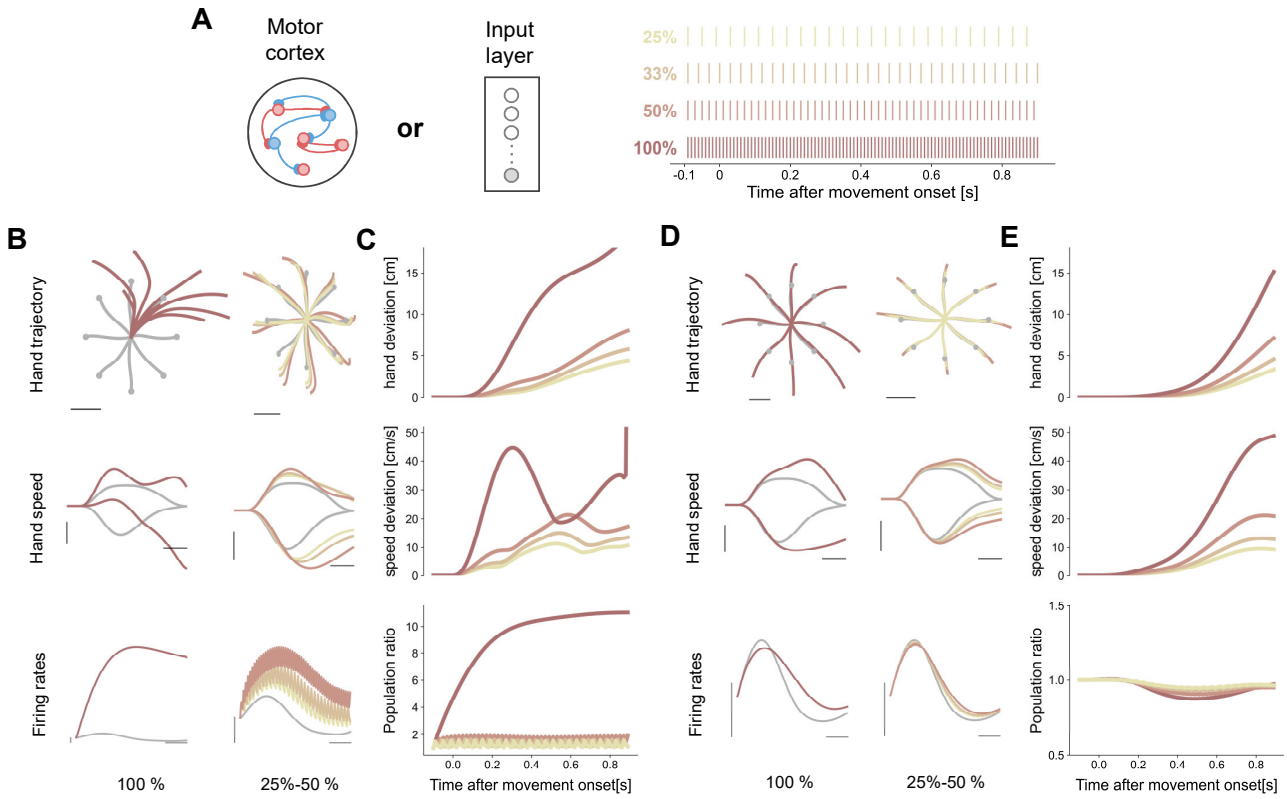

Figure 7: The contribution of the MC internal dynamics and proprioceptive feedback. (A) Illustration of graded disruption. The weights of internal recurrent connections or proprioceptive inputs was set to zero from 25% to 100% timecourse at equal time intervals, respectively. Note, the target input was preserved. (B) The influence of internal dynamics disruption on hand movement and neuronal response. 100% disruption is shown individually, while 25% - 50% are shown together. Top: hand trajectory after disruption compared to the control trial. Middle: x-y hand velocity in condition 1 after disruption compared to the control trial. Bottom: an example neurons' firing rates in condition 1 after disruption compared to the control trial. (C) The changes of hand movement and neuronal response after internal dynamics disruption. Top: condition-averaged Euclidean distance from the hand position to the control hand position at the same time point for different grades of disruption. Middle: condition-averaged Euclidean distance except for hand velocity. Bottom: population ratio that quantifies the firing rate fluctuation relative to that in control trial (D, E) Same as (B, C) except for proprioceptive feedback disruption.

beyond the disruption of internal dynamics and proprioceptive feedback. We perform the disruption strategy on the baseline model, a simplified version that dose not consider feedback delay and noise. Additionally, we find the 100% internal dynamics disruption drives the arm out of control (Figure A6), resulting in NaN in the proprioceptive feedback which cannot be estimated.

100% internal dynamics disruption impacts motor output and neuronal activity distinctly, compared to other grades. It led to obvious deviation from the original hand trajectory and irregular changes on hand velocity, suggesting internal dynamics is critical in guiding the goal of the movement (Top and middle of Figure 7B, C). The network 'explodes' without recurrent connection, reflected in a significant increase in the firing rate of single neuron and ten times activation of population responses (Bottom of Figure 7B, C). These results highlight the dominant role of internal dynamics in movement execution. On the other hand, the influence of other internal dynamics disruption increases with the grade regularly. The greater the disruption, the greater the deviation between the actual and the desire movement direction. There are strong fluctuations in neural activity, indicating the presence and absence of internal dynamics. Therefore, internal dynamics is the key determinant of motor cortical dynamics.

In contrast, there are regularities in the grades of proprioceptive feedback disruption effect motor output. Proprioceptive feedback disruption resulted in ceaseless hand movement towards the target. The greater the disruption grade, the more difficult it is to terminate the movement (Top and middle of Figure 7D, E). Moreover, proprioceptive feedback disruption had a little effect on firing rate (Bottom of Figure 7D, E), indicating that proprioceptive feedback may be more involved in fine-tuning motor commands rather than generating them.

To summarize, our result show that internal dynamics play a dominant role in generating cortical patterns, whereas proprioceptive feedback is integral to the fine-tuning of motor output.

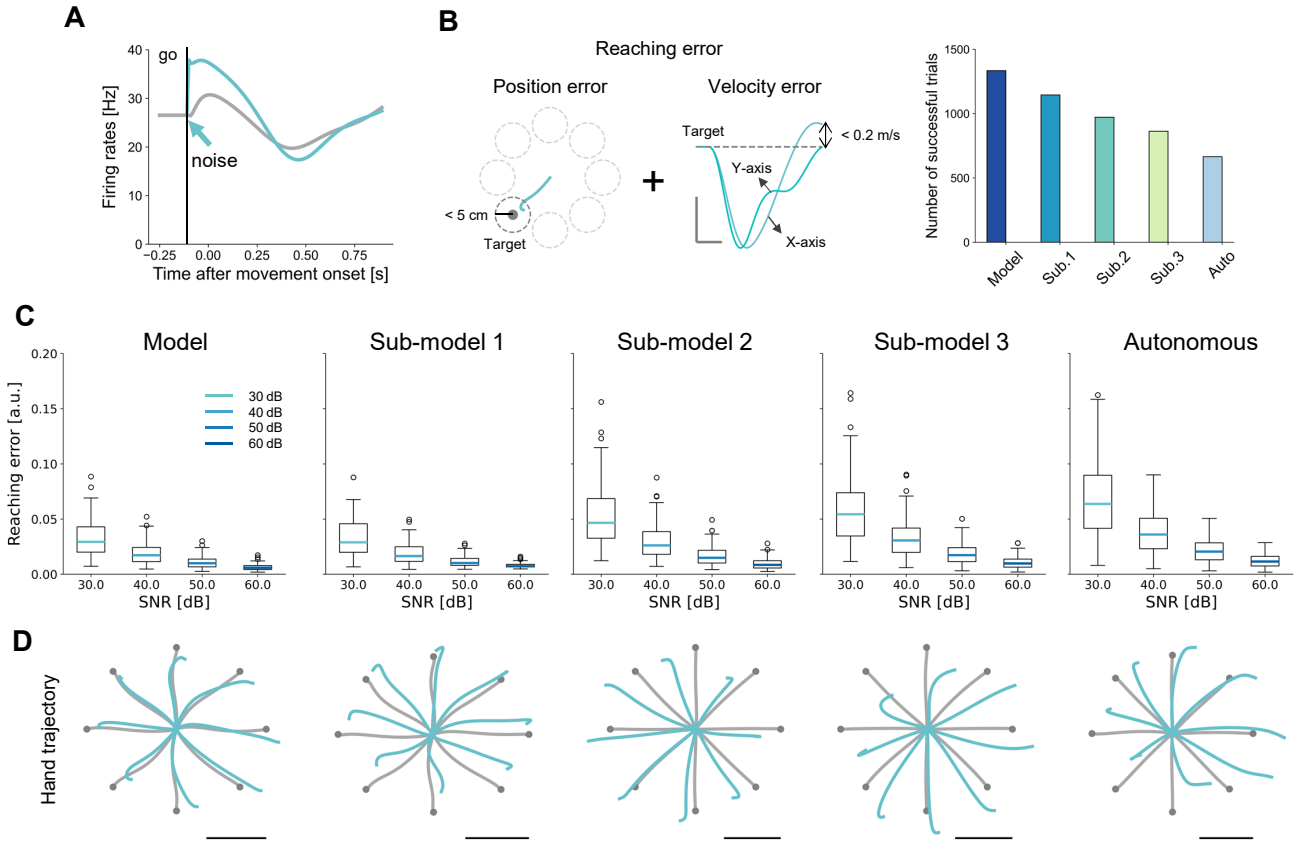

Figure 8: Proprioceptive feedback improves the robustness. (A) Illustration of noise perturbation. White Gaussian noise is provided to the initial condition (at go cue onset) of each neuron in the network. Firing rates of an example neuron (cyan) evolve after initial perturbation compared to the control trial (grey). (B) Illustration of reaching error (left) and number of successful trial of each model. (C) Box plots of the reaching error across condition. Colored lines denote the median, the boxes denote the interquartile ranges, the whiskers denote the value outside the middle 50%, and outliers denote very high value. (D) Hand trajectory after noise perturbation with a SNR of 30 dB. Only the hand trajectory at the median error in (B) is displayed. Cyan (gray) for the presence (absence) of noise in the initial condition.

3.4. Proprioceptive feedback tames sensitivity to initial condition

Initial conditions should tolerate the large neural variability; for example, different initial conditions could result in similar movements (Churchland et al., 2006, 2010). Here, we manipulated the initial conditions into an aberrant state via adding white Gaussian noise with signal-to-noise ratio (SNR) from 20-50 dB; there are 800 noisy trials corresponding to each SNR (Figure 8A). To maintain consistency with previous section (3.3), we also performed analysis on the baseline model. We perturbed the initial conditions of model, sub-models, and autonomous network model (described in 3.2) to investigate the role of proprioceptive feedback in enhancing noise robustness. Recall that sub-model 1 has no muscle force, sub-model 2 has no hand velocity, sub-model 3 only has hand position, and autonomous model has no external input. If the hand moves within a 5 cm of the target and the norm of velocity at the end of the movement is less than 0.2 within 1 second, this trial is considered a successful. The number of successful trial decrease as the number of the proprioceptive feedback decreases (Figure 8B). In the sub-models receiving two types of proprioceptive feedback, the lack of muscle force feedback generates more successful trials than lack of hand velocity feedback.

The reaching error decrease as the value of SNR increases and the number of the proprioceptive feedback increases. In particular, the condition-averaged reaching errors are comparable in model and sub-model1, but the hand trajectory corresponding to the median reaching error at 20 dB is different, where the model generates hand movement more similar to the control (Figure 8C). Also in sub-model 2 and sub-model3, lacking hand velocity feedback causes more obvious increase in reaching error than lacking muscle force, suggesting the importance of velocity feedback. The autonomous model has the poorest ability to resist initial noise, highlighting the proprioceptive feedback improved the noise robustness of network.

In conclusion, our model executed movement with acceptable deviation under different types of perturbed initial conditions. Proprioceptive feedback tames the sensitivity to initial conditions, improving the robustness of the network.

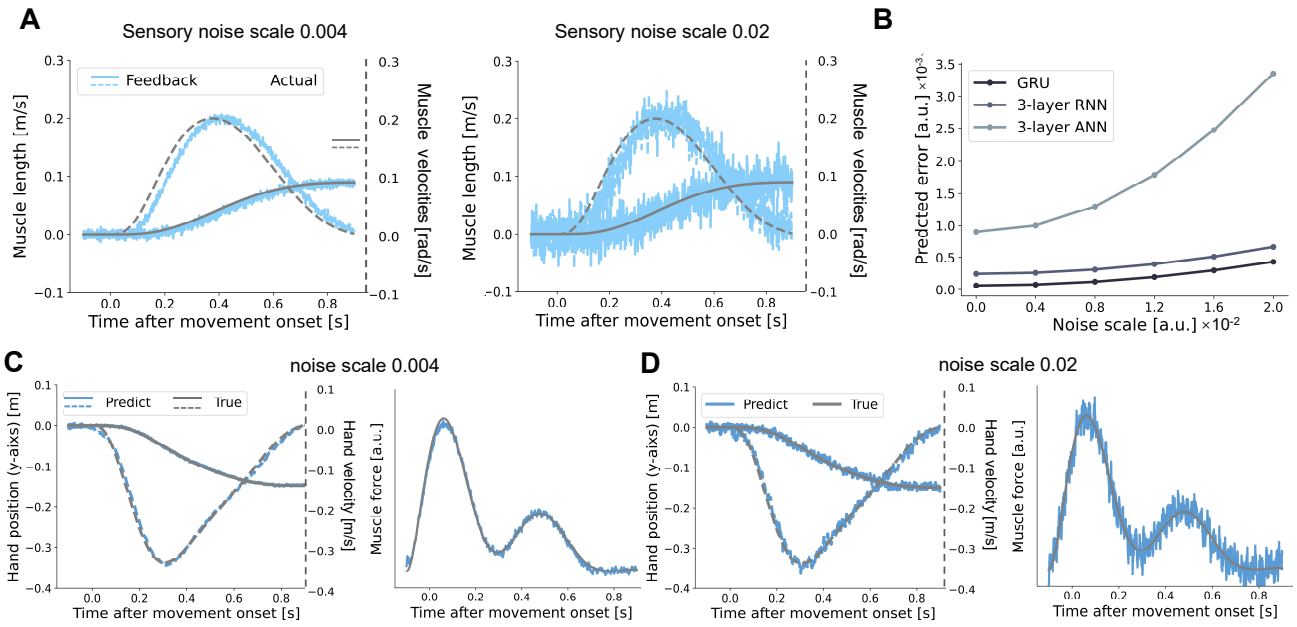

Figure 9: Estimating the arm state from proprioceptive feedback. (A) Proprioceptive feedback under different degree of sensory noise. Proprioceptive feedback includes joint angles (solid traces) and joint velocities (dashed traces). Left: the comparison of actual joint angles and velocities to proprioceptive feedback whose the variance of sensory noise is 0.01. Right: same as the left but the variance of sensory noise is 0.1. Only downward condition was shown for clarity. (B) The squared difference between the real and estimated proprioception under different degree of sensory noise. Black for GRU, dark slate gray for RNN and light slate gray for ANN. (C) Predicted proprioception in the case of sensory noise variance of 0.01. Left: the comparison of the predicted to the actual hand positions and velocities. Right: the comparison of the predicted to the actual muscle force. Only downward condition was shown for clarity. (D) Same as the (C) but the variance of sensory noise is 0.1.

3.5. Representation of proprioceptive system

In biologically realistic situations, the proprioceptive feedback is always delayed and noisy Crevecoeur et al. (2016). The proprioceptive receptors located in the arm convey muscle information instead of hand kinematics directly Proske and Gandevia (2012). We designed a sensory estimation network that considers delayed feedback and proprioceptive processing. A recent studies shows that neurons in proprioceptive system are best tuned to muscle kinematics, and the models optimized to predict the arm state best explains neural representations of proprioception (Vargas et al., 2024). Therefore, our network received the efference copies of motor command (muscle activity) and muscle length and velocity with different degree of sensory noise (Figure 9A), and then predicts position and velocity of hand and muscle force (Figure 9C, D).

Here, the noise scale s represents standard deviation of Gaussian distribution $\mathcal{N}(0, s^2)$. This network achieves high predictive accuracy for arm state (hand position and velocities, as well as muscle force) even under large sensory noise. When the noise scale is amplified 10 times, the mean squared error (MSE) is amplified 5 times, demonstrating the model's robustness (Figure 9B). Moreover, we designed other two models with deeper network layers: a three-layer-RNN and a three-layer network. The results of MSE show that the gru-based model is the best at estimating the proprioception even under large noise (Figure 9B, D). Therefore, our GRU-based sensory estimation network model accurately and robustly estimates the arm state from noisy and delayed proprioceptive feedback.

4. Discussion

Neural population dynamics have successfully explained the neural basis of movement generation. However, it remains an open question whether the population dynamics in MC are autonomously generated within the neural circuit or driven by external inputs from other brain areas. Theoretical computation found that RNNs with or without external inputs capture many prominent aspects of movement-epoch motor cortical dynamics (Hennequin et al., 2014; Kalidindi et al., 2021; Kao et al., 2021; Pandarinath et al., 2018; Suresh et al., 2020; Sussillo et al., 2015; Zimnik and Churchland, 2021). In this study, we investigated the roles of internal dynamics and proprioceptive feedback in movement execution using an RNN model to perform delayed reach task. Both of the internal dynamics and proprioceptive feedback shape the motor cortical dynamics and physical actions.

First, our model successfully simulate the neuronal activity involved in the delayed-reach task. The single-neuron peristimulus time histogram (PSTH) of model and population dynamics obtained via various dimensionality reduction techniques (PCA, dPCA and jPCA) are in good to qualitative agreement with real MC data. To quantify the similarity, we

applied CCA and Procrustes analysis to the projections of the model and neural data and found high correlation and consistency. Thus, our model strongly resembles the motor cortical dynamics, and make our analysis on the roles of internal dynamics and proprioceptive feedback convincing. We attribute the success of simulation to the advantage of ISN that is not trained for a particular movement, but contained a rich ensemble of quasi-oscillatory patterns that could be flexibly combined for the desired movement (Hennequin et al., 2014; Stroud et al., 2018). ISN aligns with the dynamical systems perspective that the MC generates a set of basic patterns for a large repertoire of movements. Moreover, unlike traditional RNN that optimized recurrent weights, we optimize the weights of initial conditions, whose number of parameters is much less than that of traditional RNN.

Second, internal dynamics predominantly govern cortical pattern generation during reaching, which is consistent with the conclusion in Bachschmid-Romano et al. (2023). In this study, disrupting internal dynamics greatly suppressed firing rates fluctuations and disrupted rotational dynamics. This may explain why many autonomous dynamical system models for the reach task achieve results similar to real data, as fast reaching movements are well pre-planned before initiation (Kao et al., 2021; Sussillo et al., 2015).

However, our findings diverge from a previous study (Kalidindi et al., 2021) in which sensory feedback contributed substantially to cortical dynamics. This difference may stem from the different methods of network analysis. First, the input during movement preparation only contains go cue signal and spatial position of the target in Kalidindi et al. (2021). This simple combination of feedforward inputs could not capture some remarkable features of preparation, such as various preparatory activity without causing movement and fast preparation(Kaufman et al., 2014; Ames et al., 2014). Theoretical work has provided strong evidence that feedforward input strategy need long time (at least 800 ms) to prepare for a movement (Kao et al., 2021). Thus, the insufficient preparation may led to bias toward the contribution of sensory feedback. Second, we employed a strategy of graded disruption (Sauerbrei et al., 2020) to dissect the contribution of proprioceptive feedback and internal dynamics. It could be rigid to infer from the amplitudes of currents generated from proprioceptive and internal dynamics source, since inputs positioned along the null-dimensions generate no output responses (Kao and Hennequin, 2019). Stavisky et al. (2017) showed that feedback-related motor cortical activity was isolated in null-dimensions that did not affect movement. Third, (Kalidindi et al., 2021) it may be inadequate to prove that network resembles motor cortical dynamics merely by the observation rotational dynamics. Rotational dynamics in the MC is widely observed during various movements, including reaching (Churchland et al., 2012), cycling (Russo et al., 2018), maintaining posture (Kalidindi et al., 2021), and even speaking (Stavisky et al., 2019). Therefore, rotational dynamics is probably a fundamental feature of motor cortical activity, but it may not evaluate a model sufficiently. There is a need for dependable evaluation index of network simulation.

Third, proprioceptive feedback interacting with internal dynamics contributes to motor cortical dynamics. Our conclusion also agrees with the recent study in the fly, where motor neurons interact with proprioceptive feedback to control movement (Gorko et al., 2024). Although proprioceptive feedback plays a modulatory role in neural population response compared to the internal dynamics, it significantly influenced behavior. We observed that disrupting proprioceptive feedback led to continuous, unceasing movement towards the target. A study found that the temporal offset in visual feedback extended deceleration duration (McKenna et al., 2017); proprioceptive feedback in our model may have similar effect. Moreover, the incorporation of sensory feedback in brain-machine interfaces has been shown to enable more efficient robotic arm control (Flesher et al., 2021; Suminski et al., 2010).

Furthermore, proprioceptive feedback enhances the network's robustness. After perturbing the initial conditions with different strategies, the network with proprioceptive feedback still reached the target with only a small deviation, especially compared to the autonomous model, which was sensitive to small differences in initial conditions. Tolerance to the variably of initial conditions is critical in any biologically network, as sensory and motor noise is present in nervous system and different initial conditions can lead to qualitatively similar movements (Churchland et al., 2006). Proprioceptive feedback tames the sensitivity to initial conditions at movement onset.

Additionally, the sensory estimation network in our study is an abstract somatosensory system, including cuneate nucleus, ventroposterior nucleus of the thalamus, and somatosensory cortex (Lutz and Bensmaia, 2021). In our study, the MC received hand position and velocity instead of the original proprioceptive feedback (joint angle and velocity) for three reasons. First, area 2 of primary somatosensory cortex encodes kinematics of the whole arm (Chowdhury et al., 2020; Vargas et al., 2024). The whole-arm model (encoding the state of hand and joints) and hand-force model (encoding the state of hand and force) (Chowdhury et al., 2020) capture the features of neural activity comparably. Second, muscle force defined in our model and force defined in Chowdhury et al. (2020) are computed differently. Third, we found the MC network receiving the combination of hand state and muscle force is more similar to real data than the network receiving the combination of hand and joints states A7.

In conclusion, our model offers a computational framework to understand the interplay between cortical internal dynamics and proprioceptive feedback during movement execution. Nevertheless, there are some limitations in our model. First, the simulation of reaction period is oversimplified in our work. We assume that sensory feedback has a limited effect, but internal dynamics and stereotyped condition-independent signal shape the population response. Second, subjects use a flexible strategy that combines visual and

proprioceptive feedback during reaching (Apker et al., 2011; Sober and Sabes, 2005), our model excluded visual feedback. Finally, our model need to be extended to more realistic and complex motor tasks to further investigate the contribution of proprioceptive feedback in movement execution.

Acknowledgements

This work was funded by the STI 2030—Major Projects (2022ZD0208604), and the National Natural Science Foundation of China (62176151 and 61773259). We are grateful to Guillaume Hennequin and Ta-Chu Kao for modeling instructions; to Juan Gallego and Matthew Perich for sharing the monkey data, and to Jieji Ren and Di Zhu for discussions.

Declaration of interest

The authors declare no competing interests.

References

Afshar, A., Santhanam, G., Byron, M.Y., Ryu, S.I., Sahani, M., Shenoy, K.V., 2011. Single-trial neural correlates of arm movement preparation. Neuron 71, 555–564.

Ames, K.C., Ryu, S.I., Shenoy, K.V., 2014. Neural dynamics of reaching following incorrect or absent motor preparation. Neuron 81, 438–451.

Apker, G., Karimi, C., Buneo, C., 2011. Contributions of vision and proprioception to arm movement planning in the vertical plane. Neuroscience letters 503, 186–190.

Bachschmid-Romano, L., Hatsopoulos, N.G., Brunel, N., 2023. Interplay between external inputs and recurrent dynamics during movement preparation and execution in a network model of motor cortex. Elife 12, e77690.

Bakken, T.E., Jorstad, N.L., Hu, Q., Lake, B.B., Tian, W., Kalmbach, B.E., Crow, M., Hodge, R.D., Krienen, F.M., Sorensen, S.A., et al., 2021. Comparative cellular analysis of motor cortex in human, marmoset and mouse. Nature 598, 111–119.

Brendel, W., Romo, R., Machens, C.K., 2011. Demixed principal component analysis. Advances in neural information processing systems 24.

Chen, A., Sun, Y., Lei, Y., Li, C., Liao, S., Meng, J., Bai, Y., Liu, Z., Liang, Z., Zhu, Z., et al., 2023. Single-cell spatial transcriptome reveals cell-type organization in the macaque cortex. Cell 186, 3726–3743.

Chowdhury, R.H., Glaser, J.I., Miller, L.E., 2020. Area 2 of primary somatosensory cortex encodes kinematics of the whole arm. Elife 9, e48198.

Chung, J., Gulcehre, C., Cho, K., Bengio, Y., 2014. Empirical evaluation of gated recurrent neural networks on sequence modeling. arXiv preprint arXiv:1412.3555 .

Churchland, M.M., Byron, M.Y., Ryu, S.I., Santhanam, G., Shenoy, K.V., 2006. Neural variability in premotor cortex provides a signature of motor preparation. Journal of Neuroscience 26, 3697–3712.

Churchland, M.M., Cunningham, J.P., Kaufman, M.T., Foster, J.D., Nuyujukian, P., Ryu, S.I., Shenoy, K.V., 2012. Neural population dynamics during reaching. Nature 487, 51–56.

Churchland, M.M., Cunningham, J.P., Kaufman, M.T., Ryu, S.I., Shenoy, K.V., 2010. Cortical preparatory activity: representation of movement or first cog in a dynamical machine? Neuron 68, 387–400.

Crevecoeur, F., Munoz, D.P., Scott, S.H., 2016. Dynamic multisensory integration: somatosensory speed trumps visual accuracy during feedback control. Journal of Neuroscience 36, 8598–8611.

Eskikand, P.Z., Soto-Breceda, A., Cook, M.J., Burkitt, A.N., Grayden, D.B., 2023. Inhibitory stabilized network behaviour in a balanced neural mass model of a cortical column. Neural Networks 166, 296–312.

Even-Chen, N., Sheffer, B., Vyas, S., Ryu, S.I., Shenoy, K.V., 2019. Structure and variability of delay activity in premotor cortex. PLoS computational biology 15, e1006808.

Flesher, S.N., Downey, J.E., Weiss, J.M., Hughes, C.L., Herrera, A.J., Tyler-Kabara, E.C., Boninger, M.L., Collinger, J.L., Gaunt, R.A., 2021. A brain-computer interface that evokes tactile sensations improves robotic arm control. Science 372, 831–836.

Gallego, J.A., Perich, M.G., Chowdhury, R.H., Solla, S.A., Miller, L.E., 2020. Long-term stability of cortical population dynamics underlying consistent behavior. Nature neuroscience 23, 260–270.

Gallego-Carracedo, C., Perich, M.G., Chowdhury, R.H., Miller, L.E., Gallego, J.Á., 2022. Local field potentials reflect cortical population dynamics in a region-specific and frequency-dependent manner. Elife 11, e73155.

Georgopoulos, A.P., Kalaska, J.F., Caminiti, R., Massey, J.T., 1982. On the relations between the direction of two-dimensional arm movements and cell discharge in primate motor cortex. Journal of Neuroscience 2, 1527–1537.

Gorko, B., Siwanowicz, I., Close, K., Christoforou, C., Hibbard, K.L., Kabra, M., Lee, A., Park, J.Y., Li, S.Y., Chen, A.B., et al., 2024. Motor neurons generate pose-targeted movements via proprioceptive sculpting. Nature , 1–8.

Hennequin, G., Vogels, T.P., Gerstner, W., 2014. Optimal control of transient dynamics in balanced networks supports generation of complex movements. Neuron 82, 1394–1406.

Herter, T.M., Korbel, T., Scott, S.H., 2009. Comparison of neural responses in primary motor cortex to transient and continuous loads during posture. Journal of neurophysiology 101, 150–163.

Inoue, Y., Mao, H., Suway, S.B., Orellana, J., Schwartz, A.B., 2018. Decoding arm speed during reaching. Nature communications 9, 5243.

Kalaska, J.F., 2019. Emerging ideas and tools to study the emergent properties of the cortical neural circuits for voluntary motor control in non-human primates. F1000Research 8.

Kalidindi, H.T., Cross, K.P., Lillicrap, T.P., Omrani, M., Falotico, E., Sabes, P.N., Scott, S.H., 2021. Rotational dynamics in motor cortex are consistent with a feedback controller. Elife 10, e67256.

Kao, T.C., Hennequin, G., 2019. Neuroscience out of control: control-theoretic perspectives on neural circuit dynamics. Current opinion in neurobiology 58, 122–129.

Kao, T.C., Sadabadi, M.S., Hennequin, G., 2021. Optimal anticipatory control as a theory of motor preparation: A thalamo-cortical circuit model. Neuron 109, 1567–1581.

Kaufman, M.T., Churchland, M.M., Ryu, S.I., Shenoy, K.V., 2014. Cortical activity in the null space: permitting preparation without movement. Nature neuroscience 17, 440–448.

Kaufman, M.T., Seely, J.S., Sussillo, D., Ryu, S.I., Shenoy, K.V., Churchland, M.M., 2016. The largest response component in the motor cortex reflects movement timing but not movement type. eneuro 3.

Kobak, D., Brendel, W., Constantinidis, C., Feierstein, C.E., Kepecs, A., Mainen, Z.F., Qi, X.L., Romo, R., Uchida, N., Machens, C.K., 2016. Demixed principal component analysis of neural population data. elife 5, e10989.

Kumar, G., Ma, C.H.E., 2023. Toward a cerebello-thalamo-cortical computational model of spinocerebellar ataxia. Neural Networks 162, 541–556.

Lillicrap, T.P., Scott, S.H., 2013. Preference distributions of primary motor cortex neurons reflect control solutions optimized for limb biomechanics. Neuron 77, 168–179.

Logiaco, L., Abbott, L., Escola, S., 2021. Thalamic control of cortical dynamics in a model of flexible motor sequencing. Cell reports 35.

Lutz, O.J., Bensmaia, S.J., 2021. Proprioceptive representations of the hand in somatosensory cortex. Current Opinion in Physiology 21, 9–16.

McKenna, E., Bray, L.C.J., Zhou, W., Joiner, W.M., 2017. The absence or temporal offset of visual feedback does not influence adaptation to novel movement dynamics. Journal of Neurophysiology 118, 2483–2498.

Michaels, J.A., Dann, B., Scherberger, H., 2016. Neural population dynamics during reaching are better explained by a dynamical system than representational tuning. PLoS computational biology 12, e1005175.

Omrani, M., Kaufman, M.T., Hatsopoulos, N.G., Cheney, P.D., 2017. Perspectives on classical controversies about the motor cortex. Journal of neurophysiology 118, 1828–1848.

Pandarinath, C., O'Shea, D.J., Collins, J., Jozefowicz, R., Stavisky, S.D., Kao, J.C., Trautmann, E.M., Kaufman, M.T., Ryu, S.I., Hochberg, L.R., et al., 2018. Inferring single-trial neural population dynamics using sequential auto-encoders. Nature methods 15, 805–815.

Perich, M., Conti, S., Badi, M., Bogaard, A., Barra, B., Wurth, S., Bloch, J., Courtine, G., Micera, S., Capogrosso, M., et al., 2020. Motor cortical dynamics are shaped by multiple distinct subspaces during naturalistic behavior (p. 2020.07. 30.228767).

Proske, U., Gandevia, S.C., 2012. The proprioceptive senses: their roles in signaling body shape, body position and movement, and muscle force. Physiological reviews .

Pruszynski, J.A., Omrani, M., Scott, S.H., 2014. Goal-dependent modulation of fast feedback responses in primary motor cortex. Journal of Neuroscience 34, 4608–4617.

Russo, A.A., Bittner, S.R., Perkins, S.M., Seely, J.S., London, B.M., Lara, A.H., Miri, A., Marshall, N.J., Kohn, A., Jessell, T.M., et al., 2018. Motor cortex embeds muscle-like commands in an untangled population response. Neuron 97, 953–966.

Safaie, M., Chang, J.C., Park, J., Miller, L.E., Dudman, J.T., Perich, M.G., Gallego, J.A., 2023. Preserved neural dynamics across animals performing similar behaviour. Nature 623, 765–771.

Sainburg, R.L., Ghilardi, M.F., Poizner, H., Ghez, C., 1995. Control of limb dynamics in normal subjects and patients without proprioception. Journal of neurophysiology 73, 820–835.

Sauerbrei, B.A., Guo, J.Z., Cohen, J.D., Mischiati, M., Guo, W., Kabra, M., Verma, N., Mensh, B., Branson, K., Hantman, A.W., 2020. Cortical pattern generation during dexterous movement is input-driven. Nature 577, 386–391.

Scott, S.H., 2004. Optimal feedback control and the neural basis of volitional motor control. Nature Reviews Neuroscience 5, 532–545.

Sergio, L.E., Hamel-Pâquet, C., Kalaska, J.F., 2005. Motor cortex neural correlates of output kinematics and kinetics during isometric-force and arm-reaching tasks. Journal of neurophysiology 94, 2353–2378.

Shenoy, K.V., Sahani, M., Churchland, M.M., 2013. Cortical control of arm movements: a dynamical systems perspective. Annual review of neuroscience 36, 337–359.

Sober, S.J., Sabes, P.N., 2005. Flexible strategies for sensory integration during motor planning. Nature neuroscience 8, 490–497.

Stavisky, S.D., Kao, J.C., Ryu, S.I., Shenoy, K.V., 2017. Motor cortical visuomotor feedback activity is initially isolated from downstream targets in output-null neural state space dimensions. Neuron 95, 195–208.

Stavisky, S.D., Willett, F.R., Wilson, G.H., Murphy, B.A., Rezaii, P., Avansino, D.T., Memberg, W.D., Miller, J.P., Kirsch, R.F., Hochberg, L.R., et al., 2019. Neural ensemble dynamics in dorsal motor cortex during speech in people with paralysis. Elife 8, e46015.

Stroud, J.P., Porter, M.A., Hennequin, G., Vogels, T.P., 2018. Motor primitives in space and time via targeted gain modulation in cortical networks. Nature neuroscience 21, 1774–1783.

Suminski, A.J., Tkach, D.C., Fagg, A.H., Hatsopoulos, N.G., 2010. Incorporating feedback from multiple sensory modalities enhances brain–machine interface control. Journal of Neuroscience 30, 16777–16787.

Suresh, A.K., Goodman, J.M., Okorokova, E.V., Kaufman, M., Hatsopoulos, N.G., Bensmaia, S.J., 2020. Neural population dynamics in motor cortex are different for reach and grasp. Elife 9, e58848.

Sussillo, D., Churchland, M.M., Kaufman, M.T., Shenoy, K.V., 2015. A neural network that finds a naturalistic solution for the production of muscle activity. Nature neuroscience 18, 1025–1033.

Todorov, E., Jordan, M.I., 2002. Optimal feedback control as a theory of motor coordination. Nature neuroscience 5, 1226–1235.

Vargas, A.M., Bisi, A., Chiappa, A.S., Versteeg, C., Miller, L.E., Mathis, A., 2024. Task-driven neural network models predict neural dynamics of proprioception. Cell 187, 1745–1761.e19.

Vyas, S., Golub, M.D., Sussillo, D., Shenoy, K.V., 2020. Computation through neural population dynamics. Annual review of neuroscience 43, 249–275.

Yu, Y., Han, F., Wang, Q., 2022. Exploring phase–amplitude coupling from primary motor cortex-basal ganglia–thalamus network model. Neural Networks 153, 130–141.

Zimnik, A.J., Churchland, M.M., 2021. Independent generation of sequence elements by motor cortex. Nature neuroscience 24, 412–424.